JGR Planets

RESEARCH ARTICLE
10.1029/2019JE006097

Key Points:
- The penetration depth of broad spectrum solar irradiation is greater in carbon dioxide ice than in water ice
- Penetration depth varies with grain size in a predictable manner, which has been modeled
- The difference in penetration depth between water and carbon dioxide ices increases with grain size

Correspondence to:
H. E. Chinnery,
hannah.chinnery@open.ac.uk

Citation:
Chinnery, H. E., Hagermann, A., Kaufmann, E., & Lewis, S. R. (2020). The penetration of solar radiation into granular carbon dioxide and water ices of varying grain sizes on Mars. *Journal of Geophysical Research: Planets*, *125*, e2019JE006097. https://doi.org/10.1029/2019JE006097

Received 19 JUN 2019
Accepted 18 MAR 2020
Accepted article online 31 MAR 2020

The Penetration of Solar Radiation Into Granular Carbon Dioxide and Water Ices of Varying Grain Sizes on Mars

H. E. Chinnery[1], A. Hagermann[2], E. Kaufmann[2], and S. R. Lewis[1]

[1]School of Physical Sciences, The Open University, Milton Keynes, UK, [2]Department of Biological and Environmental Sciences, University of Stirling, Stirling, UK

Abstract The penetration depth of broad spectrum solar irradiation over the wavelength range 300–1,100 nm has been experimentally measured for water and carbon dioxide ices of different grain size ranges. Both of these ice compositions are found on the surface of Mars and have been observed as surface frosts, snow deposits, and ice sheets. The *e*-folding scale of snow and slab ice has been previously measured, but understanding the behavior between these end-member states is important for modeling the thermal behavior and surface processes associated with ice deposits on Mars, such as grain growth and slab formation via sintering, and carbon dioxide jetting leading to the formation of araneiforms. We find the penetration depth increases in a predictable way with grain size, and an empirical model is given to fit these data, varying with both ice composition and grain size.

Plain Language Summary Most water on Mars exists as ice, both on the polar caps and in the subsurface (like permafrost on Earth). Temperatures fall low enough for carbon dioxide to also freeze. Carbon dioxide is the main constituent of Mars' seasonal polar caps. During spring, the increased sunlight results in warming within and sometimes below the ice, resulting in a "Solid-State Greenhouse Effect." This internal heating can cause the ice sheets to break up. Understanding this process requires quantifying the amount of sunlight transmitted through samples of water and carbon dioxide ice. In this paper, we have combined new and previous measurements to achieve an empirical model that predicts the penetration depth of sunlight as a function of the grain size and ice composition. This model may be used to aid the understanding of unusual ice-related features observed on the surface of Mars.

1. Introduction

Previous studies have reported the penetration depth of broad-spectrum solar irradiation in CO_2 ice in its most massive form (Chinnery et al., 2018) and at its finest, as CO_2 snow (Chinnery et al., 2019), but how do these two measurements relate to each other, and what is the behavior exhibited in between these two end-members? Is this same behavior also seen for water ice? Measurements of light penetration in water ices have been undertaken in the past, but these have used naturally occurring Antarctic snow and sea ice with all associated contaminants (e.g. Beaglehole et al., 1998; Brandt & Warren, 1993; Datt et al., 2015; Perovich, 1996), impure snow (Kaufmann & Hagermann, 2015), or the measurements were made using narrower wavelength ranges, such as France et al. (2010). Fewer previous works have investigated light penetration in CO_2 ice, but those published have also suffered from contaminants (Egan & Spagnolo, 1969) and used samples of only micrometer to several millimeters in size (Hudgins et al., 1993; Quirico & Schmitt, 1997). What has not been addressed is the relationship between the broad-spectrum penetration depth of solar radiation and ice grain size. The penetration depth, or *e*-folding scale, is defined as the depth of required to reduce the intensity of incident light to 1/e (~37%), of its initial intensity. It is an important but currently poorly constrained control on the extent of a "Solid-State Greenhouse Effect" (SSGE) induced in a surface ice deposit (Möhlmann, 2010).

In this paper, we present our findings on how the *e*-folding scale varies with grain size for both water and carbon dioxide ices. This has significant implications for understanding the evolution of the Martian seasonal and permanent polar caps, which incorporate both ice compositions in varying proportions over a wide range of grain sizes, which vary with time. It is important to understand how light penetrates into ice in all its different forms, as this leads to unique surface processes, such as CO_2 jetting (Kieffer et al., 2006). Having

constraints for the *e*-folding scale for the full range of ice grains sizes and compositions will lead to improved models and a greater understanding of the Martian surface.

1.1. Background

The Martian atmosphere consists of ~95% CO_2 and just 0.03% H_2O vapor (Gillmann et al., 2009). However, vast quantities of water ice are sequestered in the 1-km-thick northern polar residual cap, the southern polar residual cap (SPRC), and in the subsurface. CO_2 ice forms a ~10 m thick layer overlying the water ice on the SPRC; 12% to 16% of the mass of the atmosphere deposits each winter to form the seasonal CO_2 ice sheets (Genova et al., 2016), reaching a maximum thickness of 1.5 m in the north, and ~1 m in the south (Matsuo & Heki, 2009; Smith et al., 2001), although other estimates suggest up to 2 m in places (Aharonson, 2004).

Seasonal ice cap growth begins in autumn, which is thought to occur via a combination of direct deposition of CO_2 from the atmosphere to the surface, and precipitation of CO_2 snow (Kuroda et al., 2013). For the purposes of this investigation, "snow" is used to describe fine-grained ($\leq$1 mm) deposits of either water or CO_2 ice. Based on observations by the Mars Climate Sounder (MCS), Hayne et al. (2014) developed a model that suggests CO_2 snowfall contributes 3% to 20% of ice mass to the southern seasonal ice deposits at 70° to 90°S latitudes. There is likely to be very little water snow fall due to the presence of only a few precipitable micrometers (1 pr-μm 1 gm^{-2}) in the atmosphere at any one time (Spiga et al., 2017), although the Phoenix Lander observed very fine layer (μms) of water frost forming overnight (Smith et al., 2009). CO_2 ice, which initially forms as snow and frost, gradually sinters and anneals to form slab ice with high transparency and low albedo (Forget, 1998; Forget et al., 1995; Forget & Pollack, 1996). The sintering process causes grain growth and densification over time, and so the penetration depth of that ice deposit will increase as the ice becomes more translucent.

Matson and Brown (1989) first described the SSGE as the process by which subsurface heating occurs via sunlight penetrating through translucent media. Specifically, it occurs when ices are present on a planetary surface, which are translucent in the visible light range, but opaque in the infrared. This allows visible radiation to penetrate through the surface of the ice, but inhibits the re-radiation of infrared energy, often leading to the temperature maxima being located below the surface of the ice.

1.2. Ice-Related Processes and Features

The concept of the SSGE forms the basis of the CO_2 jetting model, or Kieffer model, describing the formation mechanism of "spiders" (Kieffer, 2000). Piqueux et al. (2003) were the first to define and map the distribution of spider features in the "Cryptic" region, which stretches across 73° to 81°S and is covered by seasonal CO_2 slab ice each winter (Kieffer et al., 2000). Spiders, often called araneiforms, are formed when solar irradiation is incident on a thick, low albedo CO_2 ice slab, which propagates deep into the ice, supplying energy to the underlying regolith. This process begins soon after the polar night has ended and continues throughout ice cap retreat. As the regolith warms, it reradiates energy causing basal sublimation of the CO_2 ice slab. Due to the very low porosity of the ice, CO_2 gas accumulates beneath the ice until the cryostatic pressure is exceeded and the ice slab ruptures to form a vent. If occurring under high enough pressure, venting can mobilize regolith material, which is redeposited on top of the ice slab in a fan formation. In the southern polar region, CO_2 venting has carved radial channels into the underlying bedrock, creating a weak point in the next seasonal ice cover, causing araneiforms to occur in the same places year on year (Kieffer, 2007; Kieffer et al., 2000; Kieffer et al., 2006; Martínez et al., 2012; Pilorget et al., 2011; Pilorget et al., 2013).

Seasonal furrows are similar features that have been observed in the northern polar erg. However, these are ephemeral due to sediment infill of the channels each year, blown by the summer winds that sculpt the extensive dune fields of this region (Bourke, 2013; Bourke & Cranford, 2011; Hansen et al., 2011; Hansen et al., 2013; Portyankina et al., 2017). Furrows have been observed across 95% of the northern polar dunes as well as a band across the southern hemisphere stretching from 40° to 70°S (Nash & Bourke, 2015). Furrows and araneiforms typically have a similar morphology, occurring as radially branching erosional features with a central pit, but vary with scale and longevity. Individual araneiforms can range from a few tens of meters to 1 km in diameter, with multiple interconnected branching tributaries up to 2 m deep and 5 m wide (Hansen et al., 2010; Portyankina et al., 2013), and are estimated to be in the region of 1,300–10,000 years old (Piqueux & Christensen, 2008; Portyankina et al., 2017). Seasonal furrows, on the

other hand, can also occur as "curvilinear" features and are both shallow and narrow at ~0.25 m and ~1.5 m, respectively (Bourke, 2013; Bourke & Cranford, 2011). All features, however, are thought to occur via the CO_2 jetting process and involve the transportation of material from under the ice sheet and the break up of the seasonal ice cap, requiring a solid-state greenhouse to be induced.

Other features linked to the presence of surface CO_2 ice include gullies and "Swiss cheese terrain." Gullies are geologically young features consisting of tapered channels that transport material from an upslope alcove to a basal depositional apron, often reaching several kilometers in length (Balme et al., 2006; Dickson et al., 2007; Heldmann, 2005; Heldmann et al., 2007; Heldmann & Mellon, 2004). Gullies are typically found on poleward facing slopes across the 30° to 50° latitude range in both hemispheres. The current formation mechanism for these features was proposed by Pilorget and Forget (2016), who suggest that the CO_2 jetting model (as per the Kieffer model of araneiform formation [Kieffer, 2000, 2007; Kieffer et al., 2006]) is capable of triggering mass movements when jetting is initiated on a slope.

Unusual landforms observed in the SPRC have been described as lobate features, which form a combination of troughs, mesas, and quasi-circular flat bottomed pits. These are collectively referred to as Swiss cheese terrain (Thomas et al., 2005; Thomas et al., 2009; Thomas et al., 2013). Swiss cheese terrain is associated with a layer of CO_2 ice 2–10 m in thickness, which overlies the permanent polar cap at the south pole, and its landforms are thought to be sublimation features. The "citizen science" powered study by Schwamb et al. (2018) mapped the distribution of different high latitude surface features on Mars and found that there was no location where araneiforms and Swiss cheese coexisted, and Swiss cheese only occurred within the SPRC. As the SPRC is the only place CO_2 ice is exposed all year round, which is highly eroded, higher albedo ice (Byrne & Ingersoll, 2003; Thomas et al., 2000; Thomas et al., 2013), understanding the penetration depth of smaller grained, inherently higher albedo CO_2 ice could aid in understanding the evolution of Swiss cheese terrain.

1.3. Granular Ices on Mars

Surface ice deposits of varying granularity are likely to be present due to more processes than just snowfall and frost formation. During spring, increased solar irradiation initiates the process of CO_2 jetting and the subsequent formation of araneiforms and furrows. It is also likely that increased daytime insolation could cause cracking due to thermal expansion/contraction cycles. Both of these processes result in localized break-up of the ice slab into smaller pieces.

Langevin et al. (2006) reported on the observed near-infrared spectra of the Cryptic region, obtained using the Thermal Emission Spectrometer (TES) on board the Mars Global Surveyor (MGS) and the OMEGA visible/near-infrared spectrometer on Mars Express. This region is located from 60°E to 210°E at around 80°S, and so lies within the southern seasonal polar cap and is where araneiforms are commonly observed (e.g., Schwamb et al., 2018). The strongest CO_2 ice signatures were observed in midwinter (L_s = 140°) at ~60°S. However, from soon after the spring equinox (which occurs at L_s = 180°), the seasonal cap was observed from cap edge to pole but exhibited a very week spectral signature for CO_2 ice, which is not consistent with the prevailing theory of a thick, transparent CO_2 slab in this region. Instead, the best-fit modeled spectra suggest that, from L_s = 185° to L_s = 197.3°, a surface layer of CO_2 granules ~5 mm thick, contaminated by 0.7-wt.% dust and 0.06-wt.% H_2O ice, overlies a slab of CO_2 ice approximately 150 mm thick. Following this, spectra from L_s = 223.2° are best fitted by a thin granular upper layer 0.5–1.0 mm thick consisting of 7-wt.% dust particles ~10 μm in size, 0.4-wt.% H_2O ice particles of around 10 mm in diameter, and CO_2 ice granules which protrude above the surface at 5 mm in size, again overlying a >150-mm-thick CO_2 ice slab. This level of dust contamination has the potential to inhibit araneiform formation. But by L_s = 241.9°, the CO_2 ice bands in the spectra are saturated, indicative of a clear CO_2 slab >50 mm in thickness. Kieffer et al. (2006) argue that this sequence of events actually supports the CO_2 jetting model, as, at the time of the first observations venting and subsequent dark spot/fan deposition has already been underway for ~30 sols, with much of the araneiform terrain already having reached its final configuration. The layer of granular CO_2 ice and the contamination by water ice and dust particles on the surface of a CO_2 slab is a direct result of CO_2 jetting activity and the transportation of basal regolith material to the surface.

Wind-blown dust can also be deposited on the surface of the ice, but the fact that, by L_s = 241.9°, the CO_2 slab is once again completely clean is evidence of a dust removal process. This "self-cleaning" process occurs because solar radiation is absorbed more rapidly by dust grains than by ice due to the much lower albedo

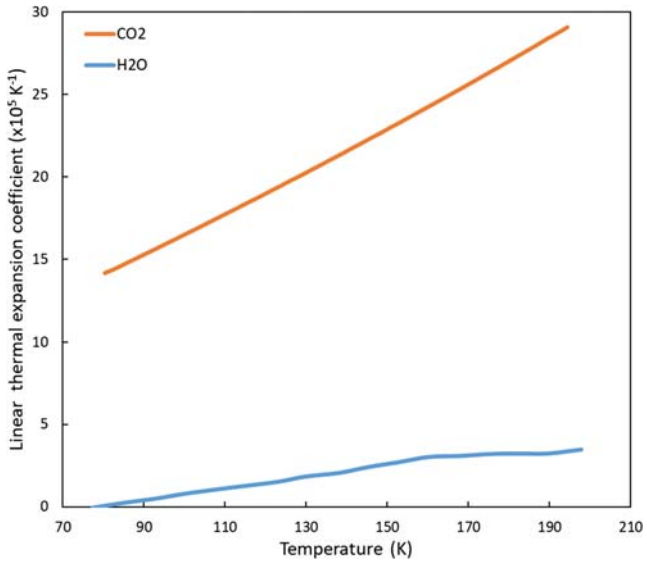

Figure 1. Linear thermal expansion coefficients ($\times 10^5$) for CO_2 ice (data from Mangan et al., 2017) and H_2O ice (data taken from Röttger et al. (2012).

of dust. The dust re-radiates this energy, initiating sublimation of the surrounding ice, which causes the grain to burrow down through the ice pack until it is ejected from the bottom of the ice or can no longer receive sufficient insolation to trigger sublimation. The burrow left behind is likely to reseal rapidly due to the overlying gas and ice receiving little heat from the grain, and so freezes, thus maintaining low slab porosity (Kieffer, 2000; Kieffer, 2007; Portyankina et al., 2010). The depth of ice to which this process occurs is dependent upon how well radiation can penetrate into the ice column, which could be modeled if the penetration depth is known.

1.4. Physical Properties of Ices

Under laboratory-controlled Martian conditions, CO_2 ice is isotropic with a cubic crystal structure, but density is temperature dependent (Mangan et al., 2017). This strong temperature dependence of density causes thermal cracking of CO_2 ice. Mangan et al. (2017) showed that the thermal expansion of CO_2 ice is much larger than for hexagonal H_2O ice over the same temperature range (80–195 K), as can be seen in Figure 1.

Over any given temperature range, CO_2 ice expands (or contracts) significantly more than water ice. Therefore, there is potential for extensive thermal cracking to occur in the seasonal CO_2 ice cap once the polar night has ended and solar radiation illuminates the ice sheet, increasing the amplitude of the diurnal temperature cycle. The strength of solid CO_2 ice is only 10% to 33% the strength of water ice under equivalent conditions (Clark & Mullen, 1976). Consequently, it is possible that slabs of CO_2 ice constrained by topography undergo internal cracking due to thermal expansion, forming granular deposits in the zones of weaknesses.

While accumulations of granular ice may not be particularly long-lived if the particles are small—microphysical models suggest surface sintering could occur rapidly, removing particles less than 1 mm in a matter of days (Clark et al., 1983; Eluszkiewicz, 1993; Eluszkiewicz et al., 2005)—larger particles or those below the immediate surface could remain stable for much longer. Sintering is the process of grain growth and densification in order to achieve the preferred thermodynamic state of minimum surface energy, and effectively changing the size of the grains, so increasing the penetration depth in those grains (Eluszkiewicz, 1993). Some fine-grained deposits have indeed been observed over longer timescales, although these are thought to be locations of frequent snowfall (Hayne et al., 2012).

In a recent experimental study by Portyankina et al. (2018), CO_2 was frozen under different pressure and temperature conditions to explore the effect on texture and ice transparency. A wide range of CO_2 ice textures formed depending on the exact P-T formation conditions, including (but not limited to) CO_2 crystals resembling snowflakes (generated at 24-mbar pressure, temperature of 160 K), a continuous translucent layer akin to slab ice (at 55-mbar pressure, temperature of 140 K), and multicrystal CO_2 ice of small hollow triangular prisms (at 7-mbar pressure, temperature of 125 K). Of particular interest was the formation of slab ice under Martian conditions for the first time, which occurred most often at pressures and temperatures close to the thermodynamic equilibrium between solid and gas phases. Under typical P-T conditions for the polar regions of Mars, CO_2 ice deposits in slab form, via a range of mechanisms and forming slab ice of varying translucency. The quality of the slab ice depends on the extent of cracking, water ice contamination, and general variations in opacity, or "cloudiness" of the ice. This indicates that while it is expected to find slab ice during both growth of the ice sheet and break up during spring from higher insolation levels, discontinuous or granular ice could be present in varying grain sizes, or with a range of effective grain sizes between cracks in the slab.

1.5. Optical Properties of Ices

Electromagnetic waves propagating in a medium are attenuated by scattering and absorption. When a homogenous, isotropic material is subjected to incident irradiation, the intensity ($\boldsymbol{I}$) of that radiation is attenuated exponentially with depth (z) through that medium:

$$I = I_0\, e^{-z/\zeta}, \tag{1}$$

where the penetration depth ζ, or *e*-folding scale, is the thickness of material required to reduce the downward directed energy to $1/e$, of its initial intensity. Theoretically, $\zeta = \frac{1}{\alpha}$, where α is the absorption coefficient.

A number of assumptions are made when applying equations of geometrical optics to actual light intensity measurements of real-world materials, especially if those are particulate materials such as granular ices. Particle size should be larger than wavelength, else a different method is required to describe the scattering behavior, for example, Mie theory or Rayleigh scattering (Bohren & Barkstrom, 1974). Light travels through granular material differently than when passing through solid material. At small grain sizes, scattering dominates; light travels via multiple reflections rather than passing through the ice, which is why snow appears white. On the other hand, solid sheets of nonporous ice are highly translucent to visible light, and so take on the appearance of the underlying material, such as in "black ice." This slab ice is observed extensively in the polar seasonal ice deposits and notably in the Cryptic region, where surface temperatures show CO_2 ice to be present, but the albedo matches that of bare regolith. Radiation intensity is only exponentially decayed by a purely absorbing material, with no internal scattering (Brandt & Warren, 1993). However, a uniform medium that both absorbs and scatters exhibits attenuation that can be approximated to an exponential decay, if the optical depth is sufficient. Kaufmann and Hagermann (2015) showed that snow reached this exponential regime after only a few millimeters, and so the use of these equations are a sufficient approximation for our experiments. A rapid decrease in light intensity through the material, whether due to scattering or absorption, will result in a small *e*-folding scale.

Generally, in materials that are highly transparent at visible wavelengths, extinction is dominated by scattering. Due to this, attenuation by particles of said material is quite different from that of the bulk solid. As long as particle size is $>\lambda$, extinction dominated by scattering is virtually independent of photon energy (Bohren & Huffman, 1983). The absorption coefficient is proportional to the scattering coefficient, which is inversely proportional to grain size d. This is because smaller grains in a fixed volume result in a greater number of scattering interfaces. However, this does not mean that the absorption coefficient or the refractive index of the bulk material should be disregarded, as absorption is fundamentally proportional to the mass of the material, while scattering is related to morphology (Schwerdtfeger & Weller, 1977). Therefore, a comprehensive model describing the penetration depth in translucent granular material would require both absorption and scattering to be accounted for.

2. Methodology

CO_2 ice samples were prepared by condensing CO_2 directly from the gas phase within a pressure vessel cooled by liquid nitrogen, following the methodology detailed in Chinnery et al. (2018) and based on that used by Kaufmann and Hagermann (2017). This formed large cylinders of CO_2 ice, which were then broken up and sieved. Water ice was made from deionized water, first boiled and then slowly frozen to minimize air bubbles in the ice. The difference between "snow" (as measured previously in Chinnery et al., 2019) and small granular ice is an important distinction, even though the grain size ranges overlap. Snow samples were made by spraying deionized water droplets into liquid nitrogen, and CO_2 snow was made using an Air Liquide Snowpack maker, connected directly to a liquid CO_2 cylinder, both of which made very fine, near-spherical droplets that tend to clump together, making grain size determination difficult (other than being sieved to <1.18 mm). Conversely, granular ice was made by processing blocks of preformed solid ice. This formation method created more angular, individual grains, analogous to what would be formed by breaking up naturally occurring ice deposits. Examples of the granular ice samples prior to sieving, therefore exhibiting a range of grain sizes and shapes, can be seen in Figure 2, where they can be compared to the alternative "snow" morphology.

Each grain size range was acquired by the use of an upper and lower mesh size sieve: For use with water ice, these were simply cooled in the freezer to approximately −40 °C, and the whole process took place inside a chest freezer to keep temperatures low and frost to a minimum; for processing CO_2 ice, the sieves were pre-cooled in a dewar vessel, with liquid nitrogen poured through them, the lid placed on, and left to cool to the temperature of the liquid nitrogen. The grains of CO_2 ice were sieved inside the dewar, therefore maintaining near-liquid nitrogen temperatures. In between samples, the sieves were removed from the dewar to

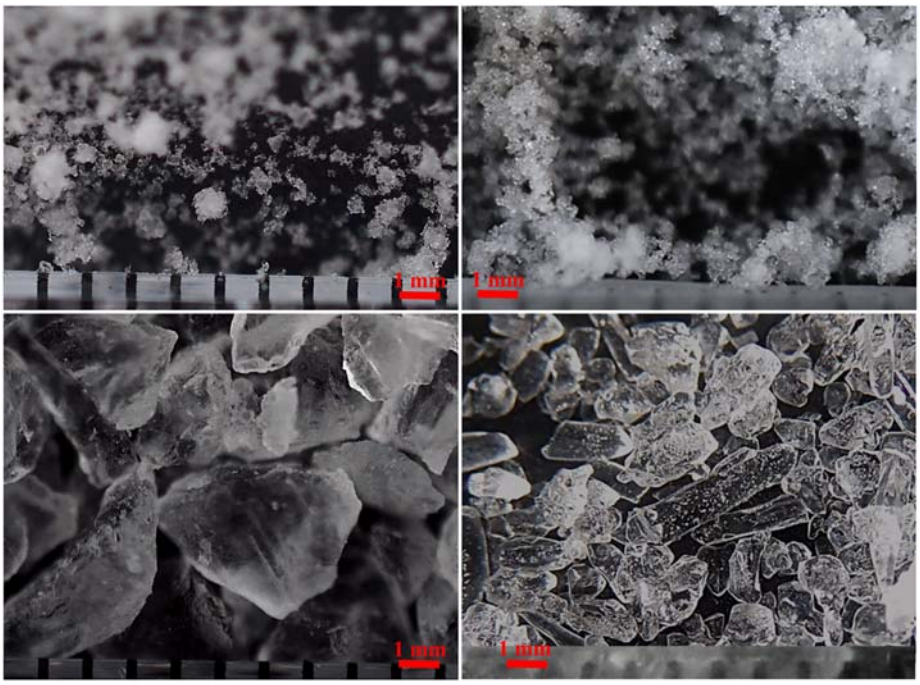

Figure 2. Top left: H_2O snow; top right: CO_2 snow; lower left, H_2O ice granules; lower right: CO_2 ice granules. All images are to the same scale. Granules are angular and irregularly shaped, but similar within each sample size range once sieved. Individual grains are of clear pure ice with little visible internal cracking or imperfections.

warm up to room temperature and left to dry completely before repeating the process. This was to remove any small amounts of frost which accumulated on the cold metal surfaces of the sieve (mostly focused on the outside walls of the sieves) due to ambient levels of moisture in the air. By repeating the chilling, sieving, warming, and drying process, instead of sieving all samples back to back, contamination by water frost was minimized. Samples were temporarily stored in a sealed insulated container in the freezer at −86 °C. This material was then treated similarly to snow for the light intensity measurements by Chinnery et al. (2019). The sieve sizes used for both the H_2O and CO_2 granular ice experiments were 0.355, 0.50, 0.60, 0.71, 0.85, 1.00, 1.18, 2.00, 3.35, 4.00, 5.60, and 8.00 mm.

Once sieved, the ice granules within each grain size range were quite similar in shape to each other, although we acknowledge there was variation in general shape between grain size ranges. Libois et al. (2013, 2014) conducted thorough investigations into the influence of grain shape on the absorption of solar radiation in terrestrial snowpacks. A wide range of naturally occurring grain shapes were identified in these studies, which were assigned values for the absorption enhancement parameter B ranging 0.7–2.4, whereas $\boldsymbol{B = 1.25}$ for spherical grains. The absorption enhancement parameter quantifies the lengthening of the photon path inside grains due to multiple internal reflections, meaning that the e-folding scale can be overestimated by ~30% in computational models when compared to real-world measurements (Libois et al., 2014). This highlights the need for laboratory measurements of the penetration depth of broad-spectrum light into snow and ice samples, rather than solely relying on theoretical models. While there is no specific control for grain shape within this study, we believe the range of shapes present within the samples is more analogous to naturally occurring samples, than using artificially spherical grains, and variations occurring to the range of grain shapes are covered within the error margins of the data.

Ice samples were held in stacked copper rings, forming a cylindrical sample container. The sample was then placed into the experimental chamber, which was accessed via a hole in the top beneath the mirror (see Figure 3). Inside, the chamber was black to prevent scattered stray light being recorded by the pyranometer and was insulated to maintain cold temperatures. Once in place, the samples were manipulated via gloves sealed into the side of the chamber. The height of the sample could be decreased in 5 mm increments by removing individual copper rings, and then scraping the sample surface flat using a silicone spatula

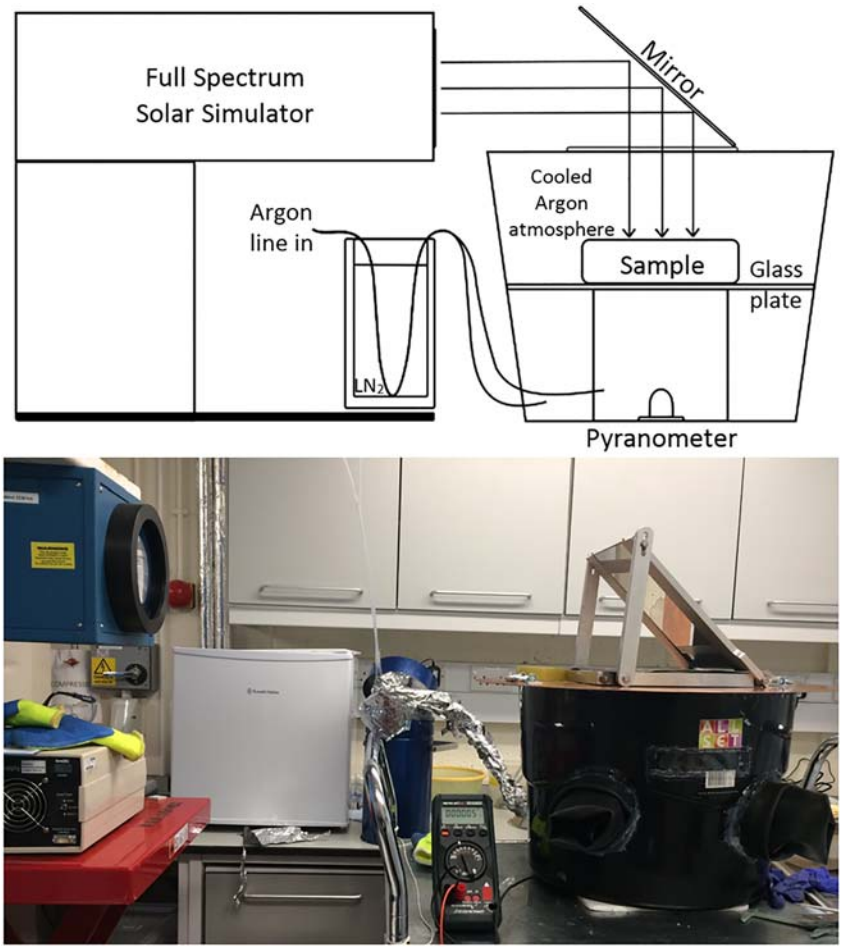

Figure 3. Equipment and experimental set-up used to conduct all light intensity measurements.

across the top of the sample holder. By using this method, the volume of ice was kept consistent from sample to sample. Ice samples were irradiated using a solar simulator lamp (model LS1000R3, Solar Light Company), which utilizes a Xenon arc lamp and specialized filters to closely match the full spectral radiance of the sun in space. Therefore, this is a good approximation for the radiation received on Mars, excluding any minor effects from Mars's atmospheric composition, clouds or suspended dust. Light from the lamp is directed via the mirror to be incident perpendicular on the surface of the sample (see experimental configuration shown in Figure 3). Light intensities were recorded using a multimeter connected to the pyranometer (CS300, Campbell Scientific Ltd.), which is sensitive across the wavelength range of 300–1,100 nm placed directly beneath the sample, in the center of the directed light beam. Measurements were made at four points for each sample thickness: once in the center, then three radially around that central point. The mean of these measurements was determined and used to calculate the *e*-folding scale of each sample, in order to minimize the effect of any inhomogeneities (such as slight density variations, etc.). After the four measurements had been recorded at each given thickness, the top copper ring was removed, the sample scraped off again, and light intensity measurements commenced. This process was repeated as necessary, in 5 mm thickness increments, and was all conducted inside the chamber flooded with cooled argon gas, which minimized both sintering and water frost contamination of the samples.

It was not deemed necessary for the measurements to be performed under Martian conditions for two reasons. Firstly, by calculating the *e*-folding scale from light intensity measurements at different thicknesses, the relative change in intensity is the defining variable, not the absolute light intensity. Because of this, terrestrial atmospheric pressure and composition would have made no measurable difference to the results, as

Table 1
Granular Ice Depth Ranges Over Which the e-Folding Scale was Derived

Grain size range (mm)	Depth of measurements used to calculate *e*-folding scale (mm)	
	CO_2	H_2O
0.355–0.50	5–10	5–10
0.50–0.60	5–10	5–10
0.60–0.71	5–10	5–10
0.71–0.85	5–10	5–10
0.85–1.00	5–10	5–10
1.00–1.18	5–10	5–10
1.18–2.00	5–15	5–15
2.00–3.35	5–20	5–20
3.35–4.00	10–25	10–25
4.00–5.60	10–30	10–30
5.60–8.00	10–30	10–30

Note. The starting depth/"zero point" and the range of ice depth increased with larger grain sizes due to lower albedo and greater transparency of the sample.

long as conditions remained constant for the duration of the experiment. Secondly, throughout the course of the measurements, access was required to directly manipulate the samples, which would be very difficult if conducted within a vacuum chamber. As a consequence, efforts were taken to minimize the presence of water vapor, and maintain the cold temperatures required to keep the samples stable.

3. Results

The four results from the light intensity measurements at each sample thickness were averaged to give a mean light intensity per granular ice sample, per ice depth. Because reliable albedo measurements are difficult to obtain, only measurements taken at depths greater than that required to eliminate any possible albedo variations were used. In accordance with the methodology used by Kaufmann and Hagermann (2015), for small ice grains, the measurements taken at 5-mm depth were used as the zero point and subsequent values normalized accordingly (so that calculations are made over the change in ice thickness, rather than absolute thickness). However, in our previous study (Chinnery et al., 2018), it was found that a minimum ice depth of 8 mm was needed to remove the effects of albedo from slab ice measurements, and a greater range of ice thickness measurements was required due to the increased transparency of compact ice. The granular ice samples were measured in increments of 5 mm due to the copper ring sizes used to adjust sample height, and so at larger grain sizes, the reference depth was increased to 10 mm, and depth range was also increased (see Table 1). The normalized values were then used to calculate the *e*-folding scale for those grain sizes, using equation 2, where the downward directed energy flux ($\boldsymbol{F}$) is a function of ice thickness ($\boldsymbol{x}$) and the penetration depth, or *e*-folding scale ($\boldsymbol{\zeta}$).

$$\boldsymbol{F}(\boldsymbol{x}) = \boldsymbol{e}^{-\boldsymbol{x}/\zeta}. \tag{2}$$

The resulting *e*-folding scales for granular CO_2 and H_2O ice have been plotted in Figures 4 and 5, respectively. The horizontal error bars on both plots denote the range of grain sizes used in each experimental sample, and the vertical errors for the *e*-folding scale are an estimate based on experimental error, including device tolerance and human error. Generally, the penetration depth increases with increasing grain size, as would be expected, but not linearly.

In both types of ice, but most pronounced with CO_2 ice, there is greater data scatter at the smallest grain sizes. This is due to several factors: The smaller the grain size, the more rapid the sintering rate, and due to the volatility of CO_2, this was a greater effect. While efforts were made to minimize this (e.g., using samples as quickly as possible after preparation, storing for the short periods required using liquid nitrogen to cool the samples, flooding the experimental chamber with cooled argon gas), it is likely that some sintering occurred when the grains were exposed to irradiation from the solar simulator. Similarly, with the smallest grains of water ice, a small amount of melting occurred when the solar simulator lamp was in operation. The chamber was cooled, but not to such cold temperatures as was used for CO_2 ice measurements. This is because, during testing, cooling the chamber too much caused the grains in contact with the glass base to stick and made collecting multiple measurements difficult. All these issues were significantly less in the larger ice grain sizes. Due to this, we estimate the data errors on grain sizes <1.18 mm to be ±3 mm, as used for the snow *e*-folding scale measurements by Chinnery et al. (2019), but for the larger grains >1.18 mm ±2 mm.

4. Analysis

The penetration depth in ices is highly wavelength dependent, primarily because the absorption coefficient of bulk ice can vary by many orders of magnitude across the visible wavelength range. If grain size remains constant, then the penetration depth decreases with increasing wavelength. This is evidenced by the results

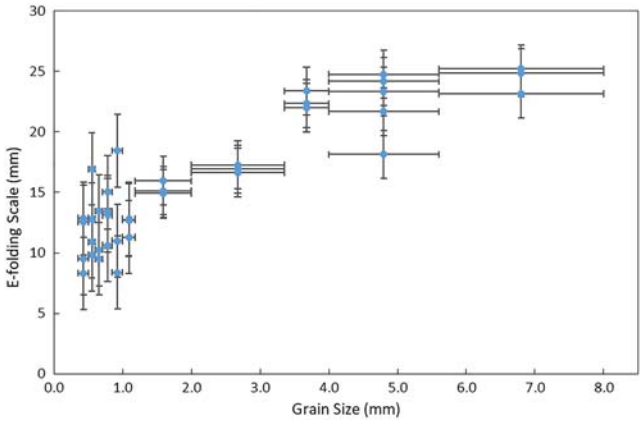

Figure 4. Results from light intensity measurements showing how the *e*-folding scale of granular CO_2 ice increases with increasing grain size.

of Perovich (1996) for the penetration depth of sea ice at different wavelengths, which ranged from 24 m at λ = **470 nm**, 2 m at λ = **700 nm**, to 0.05 m at λ = **1,000 nm**. It therefore follows that, as the penetration depth, ζ, is proportional to grain size, d, if wavelength, λ, is held constant the penetration depth will increase with increasing grain size. Li et al. (2001) used this principle to model the penetration depths of different wavelengths in a 1-m-thick snowpack as would be detected by the AVIRIS (Airborne Visible/Infrared Imaging Spectrometer) instrument. If we select the results from their model which are applicable to our wavelength range (300–1,100 nm), the penetration depths are plotted in Figure 6, alongside a trendline for each wavelength specific relationship.

When plotted, the relationship between the data in Figure 6 follows the trend line:

$$y = a\,x^{0.5}, \tag{3}$$

with a being wavelength dependent, y the penetration depth, and x grain size. Equation 3 forms the basis of the model derived here for H_2O and CO_2 ice granules. An iterative least-squares method was used to determine an empirical fit for the value of a, which was found to be constant for both ice compositions, based on the numbers retrieved by separate analysis for each ice composition being near equal, and the fact that the penetration depth of snow is the same for both compositions. This is logical given that the wavelength range used to irradiate the samples is constant for all measurements made (but it is this factor that varies with wavelength for the Li et al., 2001, data). However, if a is constant then grain size, x, must be scaled by a factor that is dependent on ice composition. This is because x should equal the effective diameter of nonspherical snow grains, which would be significantly smaller than the actual ice grain radius due to scattering from small internal features (Domine et al., 2008). Therefore, theoretically x should be scaled by a factor related to the scattering and absorption coefficients and so would be compositionally specific. However, as the measurements presented here are made over a broad spectral range of 300–1,100 nm, and the absorption coefficient for water and carbon dioxide ice increases by several orders of magnitude over these wavelengths, it would require integrating these values across these wavelengths and much more detailed measurements to derive this scaling factor theoretically from first principles. The iterative least squared process was repeated to determine the scaling factor, and x is substituted in the equation by grain diameter d and the scaling factor b.

The retrieved value of the scaling factor for water ice, rounded to the same number of significant figures $b \approx 0.031$. Schwerdtfeger and Weller (1977) made measurements of downwards-directed flux in naturally occurring snows at Plateau Station in Antarctica, and they determined from their data that the asymptotic flux extinction coefficient μ equals 0.030 scaled by grain diameter, d. Schwerdtfeger and Weller (1977) gave equation 4 as the relationship for calculating the light intensity I at a given depth of material z:

$$I = I_0\,e^{(-\mu z)}. \tag{4}$$

Comparing equation 1 with equation 4, it is clear that $\mu z = z/\zeta$, therefore $\mu = 1/\zeta$ (Domine et al., 2008). As $\mu z = 0.030/d$ (Schwerdtfeger & Weller, 1977), then $\zeta = d/0.030$. However, this simple relationship also does not explain our data on its own, but given the insignificant difference between this value and that retrieved by Schwerdtfeger and Weller (1977), for the purposes of this study and the ability to predict the penetration depth of broad-spectrum solar irradiation in either water ice, this relationship can be substituted into our equation and 0.03 used as the scaling factor for water ice. There is no previous

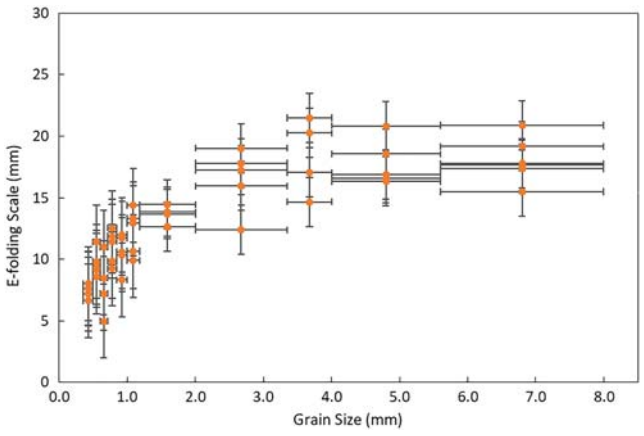

Figure 5. Results from light intensity measurements showing how the *e*-folding scale of granular H_2O ice increases with increasing grain size.

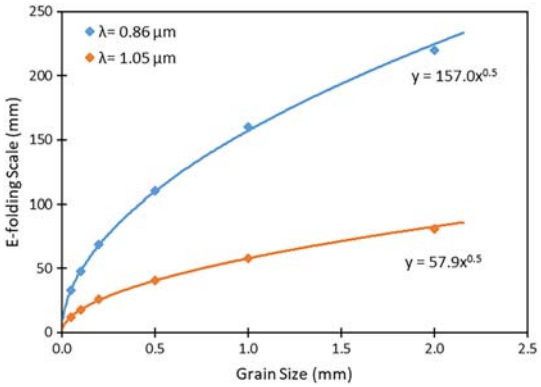

Figure 6. Selection of data based on applicable wavelength range from Li et al. (2001): Penetration depths in snow of specified grain size at specific wavelengths. Trend lines fitted via least-squares method.

work to guide the scaling factor of CO_2 ice, and so we simply use the value retrieved by the least-squares method.

The dependence of the *e*-folding scale on grain size can be approximated by using the following equation, which can be seen plotted alongside the measurements in Figure 7:

$$\zeta = a + \left(\frac{d}{b}\right)^{0.5}, \quad (5)$$

where $a = 5.370$, $b_{H2O} = 0.030$, $b_{CO2} = 0.0144$, and d= diameter of ice grain.

This formula (equation 5) provides an improved representation of the data for the broad spectrum measurements presented in this study.

This model is applicable for use across the visible spectrum, including the near IR and near UV, for wavelengths 300–1,100 nm, and up to a limited grain size, above which could be deemed to be slab ice (although at which point this occurs is still a matter for debate). Of itself, it does not take wavelength into account. As both the refractive index *n* and the absorption coefficient α are wavelength dependent, the ideal would be for these to be substituted into this equation. However, with our limited data, we are unable to do this. The measured *e*-folding scales for granular ice, as presented in this study, are plotted in Figure 7. Additionally, the *e*-folding scale of CO_2 slab ice, from Chinnery et al. (2018), and for both CO_2 and H_2O snow (Chinnery et al., 2019) are also plotted in this graph.

So that direct comparisons can be made between ice compositions, light intensity measurements using slabs of water ice have also been undertaken, following the same methodology used for the CO_2 ice measurements (as detailed in Chinnery et al., 2018). The model gives a good prediction of the *e*-folding scale up to the point at which slab ice is plotted. The "effective grain size" was chosen for slab ice via digital analysis of photographs of the sample using the software ImageJ (Schneider et al., 2012), with the smallest distance between cracks measured to be approximately 10 mm, and the largest 40 mm, while the effective grain size in water ice samples were determined to be larger at 15–45 mm. The lower panel of Figure 7 gives two examples of CO_2 slab ice samples, and two examples of H_2O slab ice samples (of eight which were analyzed). Many of the water ice samples exhibited bubbles in the middle, and so measurements made in the center of these samples (method exactly followed that of CO_2 slab ice measurements) were excluded from analysis when calculating the *e*-folding scale.

This model is a first approximation for quantifying the relationship between the penetration depths of broad-spectrum solar radiation in granular ice of different compositions. More extensive measurements are required to refine it further, with the aim of allowing for the optical properties of the ices to be fully integrated into the equation. This could also aid in defining an upper grain-size boundary, where the *e*-folding scale would plateau and remain constant as would be applicable for the seasonal slab ice deposit observed during early spring in the Cryptic region of the southern polar cap.

5. Discussion

Results for the *e*-folding scale for granular ice deposits fit well with the previously published snow and slab ice results of $\zeta_{snow} = 11.2 \pm 3$ **mm** (Chinnery et al., 2019), and on average $\zeta_{CO2\ slab} = 47.6 \pm 2$ **mm,** ranging up to **65.1 ± 6.3 mm** for the best quality ice samples (Chinnery et al., 2018). Further to this, Portyankina et al. (2018) made light intensity measurements over the wavelength range 450–900 nm in CO_2 ice formed under Martian pressure and temperature conditions, which we have used to calculate the penetration depth of $\zeta_{CO2\ slab} = 66.7$ **mm**. This is in good agreement with the upper range for the penetration depth of CO_2 slab ice as measured in our previous experiments, despite the slightly narrower wavelength range used. It is likely that the Portyankina et al. (2018) results are slightly higher than those from Chinnery et al. (2018) due to the improvements in temperature and atmospheric control (therefore reducing imperfections within the ice), but it is nonetheless consistent within the error margins of our work. For both water and carbon dioxide

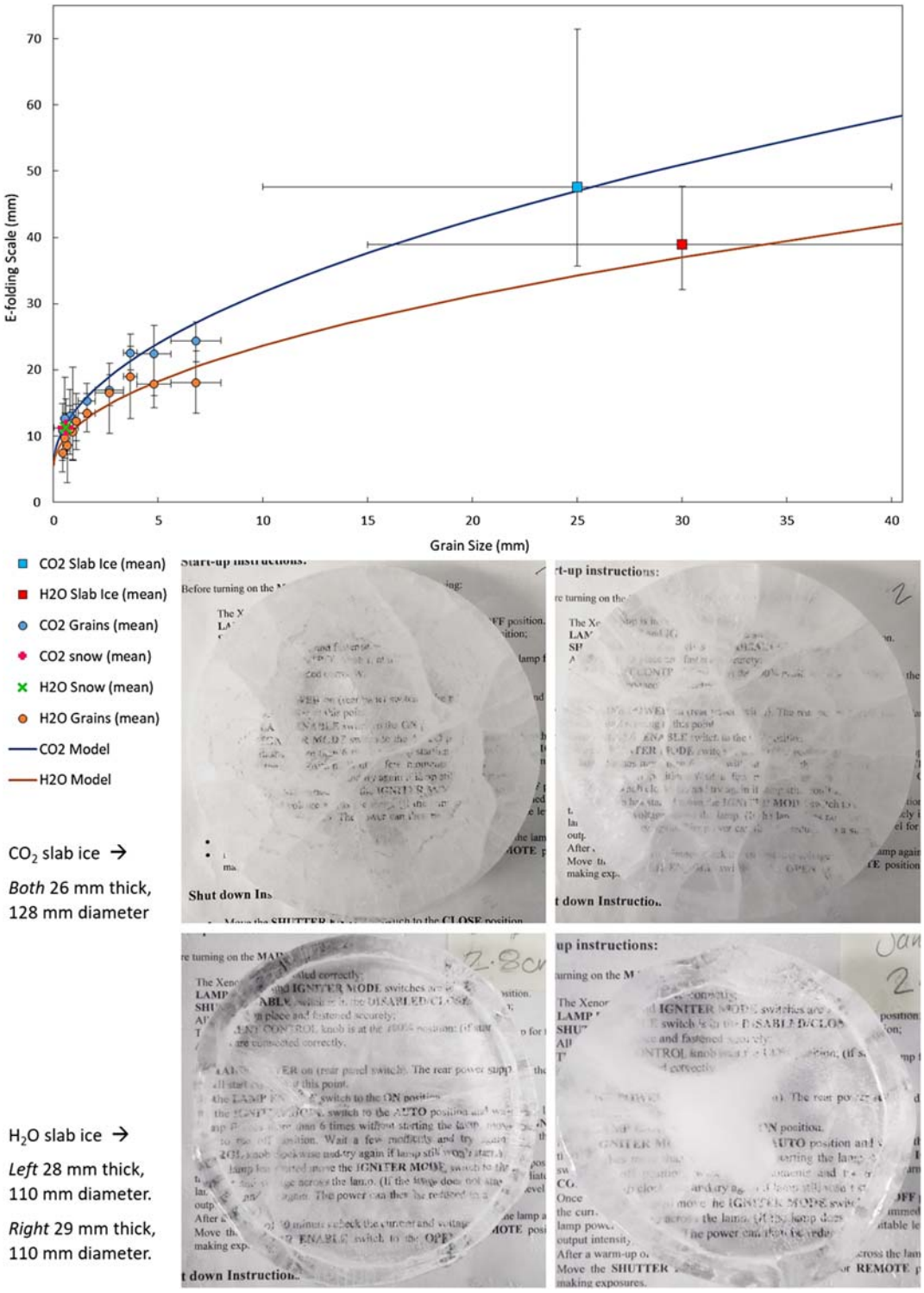

Figure 7. Top: The average (mean) *e*-folding scale is plotted for each grain size and ice composition. The *e*-folding scale of H_2O and CO_2 snow is plotted (data from Chinnery et al., 2019), in addition to the results from slab ice experiments, of which the CO_2 slab ice *e*-folding scale was published in Chinnery et al. (2018). Vertical error bars show the spread of data ±2 mm for experimental errors, horizontal errors denote the grain size ranges. Note that both CO_2 and H_2O snow plot at the same location on the graph at 11.2 mm ±3 mm (see Chinnery et al., 2019 for details). Bottom images: examples of CO_2 (upper) and H_2O (lower) slab ice samples, which were digitally analyzed to determine the "effective grain size range" of the samples in order to plot on the graph as horizontal error bars.

Table 2
The e-Folding Scale of a CO_2 Granular Ice Deposit, Based on the e-Folding Scale Grain Size Model, and the Associated Reduction in Insolation Intensity at the Base of the Ice Deposit Compared to the Surface

Grain size (mm)	*e*-folding scale (mm)	Ice depth	Insolation reduction	References for grain size and ice thickness
0.001	5.63	0.1 mm	1.76%	Piqueux et al. (2016)
		0.5 mm	8.50%	
0.10	8.01	10 mm*	71.30%	Hayne et al. (2014)
5.00	24.00	10 mm*	34.08%	Langevin et al. (2006); Langevin et al. (2007)
10.0	31.72	10 mm*	27.04%	Kieffer (2000); Langevin et al. (2007)
100	88.70	10 mm	10.66%	Langevin et al. (2007)
200	123.22	0.2 m	80.27%	Langevin et al. (2007); Mitrofanov, et al. (2003)
		0.5 m	98.27%	Langevin et al. (2007))
		1.0 m	99.97%	Kieffer (2007)
500	191.71	0.5 m	92.63%	Langevin et al. (2007)
		1.0 m	99.46%	Kieffer (2007); Mitrofanov et al. (2003)
		1.5 m	99.96%	Matsuo and Heki (2009); Smith et al. (2001)

.*Note*. Asterisk symbol (*) denotes where no ice depth estimate was available, so 10 mm has been used for comparison purposes.

ice, there is a clear trend from a regime of light propagation in ice composed of grains of the smallest sizes (snow, grain size $\leq$1 mm) to slab ice (grain size $\rightarrow \infty$), although the point at which it would be appropriate to transition from the "grain size" model to slab ice regime is difficult to define, depending on how unblemished the slab ice is. Further measurements utilizing samples of larger grains (>8 mm), and of narrower grain size ranges, of CO_2 and H_2O ices would help determine this. However, the measurements and model of the *e*-folding scale have applications for all instances of granular ices on planetary bodies, including Earth, comets, and icy moons, in addition to Mars.

Specifically, accurate knowledge of light transmission through ice is needed for heat transfer models, which can reliably predict surface atmosphere interactions on Mars when involving surface ice, such as frosts, snow falls, sintered snow, and sintering rates as snow is metamorphosed into solid ice. This last point is particularly interesting, as the more sintered a snowpack becomes, the larger the effective grain size, and so the penetration depth increases. The resulting effect is that more visible light can penetrate through to the underlying regolith, although, if bulk porosity is decreased, more infrared wavelengths are absorbed by the ice itself due to the absorption bands exhibited by solid CO_2 (Warren, 1986; Quirico & Schmitt, 1997; Hansen, 2005). Thermal models, such as the study by Pilorget et al. (2011) of CO_2 jetting in the seasonal ice sheet, use theoretical values of penetration depths based on the optical properties of CO_2 ice and Mie scattering theory. These models are valuable tools but make a number of assumptions, including constant ice grain size and shape, with no density fluctuations and perfect uniformity to slab ice deposits, and are therefore likely to significantly overestimate the penetration depth in naturally occurring ices. While the samples used in this study did not have a strict control on many of these factors, variations in grain shape and the presence of a small number of gas bubbles in the ice are much more likely to be analogous to naturally occurring, in situ ice deposits rather than idealized models.

Table 2 details the predicted *e*-folding scale values for a range of different CO_2 ice grain sizes, which have been observed and/or inferred on the surface of Mars (detailed in section 1.3). The amount of incident sunlight that could penetrate through to the base of the ice has been calculated as a percentage of the insolation received at the surface of the ice. The actual extent of subsurface warming and whether this would lead to basal sublimation depends on many factors, not least the intensity of received insolation, thermal and mechanical properties of the underlying regolith, local temperature and pressure conditions, and so forth, which is beyond the scope of this study. However, it can be seen from these calculations that even a very fine covering of frost, for example, a 0.5-mm-thick deposit of grains 1 μm in diameter reduces insolation by 8.5%, which could have significant implications for quenching CO_2 jetting if frost forms on top of a CO_2 slab. Fine grained CO_2 ice could be deposited on top of the ice by the jetting process itself via adiabatic cooling of the gas jets, which then settles out on the slab surface.

At the largest "effective grain size" of 0.5 m for a 1.5-m-thick CO_2 slab, these estimates suggest only 0.04% of surface radiation reaches the bottom of the ice (not taking into account the potential error range of these

data), which may not be sufficient to initiate basal sublimation and araneiform formation. These measurements could be used to put an upper constraint on ice thickness in regions where CO_2 jetting is active, or perhaps invoke a requirement for a certain proportion of absorbing impurities within the ice to induce sublimation within the ice itself.

Further work to refine this model would be beneficial, conducted by measuring the penetration depth in a range of different ices that occur on other planetary bodies in the solar system, such as methane, or icy mixtures. Furthermore, this would be improved by a greater range of more narrowly constrained grain size measurements and having improved thermal control over the ice samples, which would enable light intensity measurements in more pristine ice slabs, allowing for the maximum *e*-folding scale to be determined and placing an upper boundary on the model. Other aspects that could be integrated into the model would be the effect of contaminants, such as the measurements performed by Kaufmann and Hagermann (2015), who used Mars simulant JSC-1A to contaminate water snow samples and determine the effect on the penetration depth of broad-spectrum solar irradiation. If this were to be conducted using CO_2 snow then this would greatly improve our understanding of how the Martian polar regions behave, and further improve the modeling of araneiform and gully formation, for example.

6. Conclusions

The penetration depth of broad-spectrum (300–1100 nm) solar irradiation in granular ice has been calculated from light intensity measurements through water and carbon dioxide ices of different grain sizes. This was brought together with previous results giving the *e*-folding scale of H_2O and CO_2 snow, CO_2 slab ice, and new measurements of H_2O slab ice. It has been found that the penetration depth varies with both grain size and composition in a manner that has been modeled within this study. It was found that while the penetration depth at small grain sizes (approximately $\leq$1 mm in diameter) is the same within the margins of experimental error, as grain size increases, the impact of ice composition becomes more important. This is due to a greater proportion of light propagation occurring as transmission through the grains as opposed to scattering at the grain surfaces. As a consequence, the material properties of the ice, such as the refractive index and absorption coefficient, influence the penetration depth, alongside an inverse correlation with grain size. At larger grain sizes, increasing up to slab ice, the data clearly show larger *e*-folding scales for CO_2 ice than H_2O ice. These results can be used to refine parameterization of radiative transfer models for surface-atmosphere interactions for any planetary surface that hosts either water or carbon dioxide ice. This is particularly relevant to the polar regions of Mars, where both water and carbon dioxide ices are present on the surface, but unique surface processes, such as CO_2 jetting, which gives rise to araneiforms, are only observed in the presence of CO_2 ice. A consistently higher *e*-folding scale of large grained carbon dioxide ice instead of water ice is a good explanation of these observations, as there is more energy from solar irradiation able to reach the underlying regolith, causing an enhanced solid-state greenhouse effect when compared to water ice.

Acknowledgments
The authors would like to thank the reviewers for their comments and suggestions, which have greatly improved this manuscript. This work was funded by STFC under grant ST/N50421X/1 with additional support from grants ST/S001271/1 and ST/P000657/1, and UKSA grants ST/R001405/1 and ST/S00145X/1. Access to the full dataset from these experiments can be found in the online data repository of The Open University (https://doi.org/10.21954/ou.rd.9896084.v1).

References

Aharonson, O. (2004). Depth, distribution, and density of CO_2 deposition on Mars. *Journal of Geophysical Research*, *109*(E5). https://doi.org/10.1029/2003je002223

Balme, M., Mangold, N., Baratoux, D., Costard, F., Gosselin, M., Masson, P., et al. (2006). Orientation and distribution of recent gullies in the southern hemisphere of Mars: Observations from High Resolution Stereo Camera/Mars Express (HRSC/MEX) and Mars Orbiter Camera/Mars Global Surveyor (MOC/MGS) data. *Journal of Geophysical Research*, *111*(E5).

Beaglehole, D., Ramanathan, B., & Rumberg, J. (1998). The UV to IR transmittance of Antarctic snow. *Journal of Geophysical Research: Atmospheres*, *103*(D8), 8849. https://doi.org/10.1029/97jd03604

Bohren, C. F., & Barkstrom, B. R. (1974). Theory of the optical properties of snow. *Journal of Geophysical Research*, *79*(30), 4527–4535.

Bohren, C. F., & Huffman, D. R. (1983). *Absorption and scattering of light by small particles*. New York: Wiley-Interscience.

Bourke, M., and A. Cranford (2011), Seasonal formation of furrows on polar dunes, in Fifth Mars Polar Science Conference, edited.

Bourke, M. C. (2013), The formation of sand furrows by cryo-venting on martian dunes, in 44th Lunar and Planetary Science Conference, Edited.

Brandt, R. E., & Warren, S. G. (1993). Solar-heating rates and temperature profiles in antarctic snow and ice. *Journal of Glaciology*, *39*(131), 99–110.

Byrne, S., & Ingersoll, A. P. (2003). A sublimation model for Martian south polar ice features. *Science*, *299*(5609), 1051–1053. https://doi.org/10.1126/science.1080148

Chinnery, H. E., Hagermann, A., Kaufmann, E., & Lewis, S. R. (2018). The penetration of solar radiation into carbon dioxide ice. *Journal of Geophysical Research: Planets*, *123*(4), 864–871. https://doi.org/10.1002/2018je005539

Chinnery, H. E., Hagermann, A., Kaufmann, E., & Lewis, S. R. (2019). The penetration of solar radiation into water and carbon dioxide snow, with reference to Mars. *Journal of Geophysical Research: Planets*, *124*(2), 337–348. https://doi.org/10.1029/2018je005771

Clark, B. R., & Mullen, R. P. (1976). Martian glaciation and the flow of solid CO_2. *Icarus*, *27*, 215–228.

Clark, R. N., Fanale, F. P., & Zent, A. P. (1983). Frost grain size metamorphism: Implications for remote sensing of planetary surfaces. *Icarus*, *56*, 233–245.

Datt, P., Gusain, H. S., & Das, R. K. (2015). Measurements of net subsurface heat flux in snow and ice media in Dronning Maud Land, Antartica. *Journal Geological Society of India*, *86*, 613–619.

Dickson, J. L., Head, J. W., & Kreslavsky, M. (2007). Martian gullies in the southern mid-latitudes of Mars: Evidence for climate-controlled formation of young fluvial features based upon local and global topography. *Icarus*, *188*(2), 315–323.

Domine, F., Albert, M., Huthwelker, T., Jacobi, H.-W., Kokhanovsky, A. A., Lehning, M., et al. (2008). Snow physics as relevant to snow photochemistry, atmospheric chemistry and physics. *European Geosciences Union*, *8*(2), 171–208.

Egan, W. G., & Spagnolo, F. A. (1969). Complex index of refraction of bulk solid carbon dioxide. *Applied Optics*, *8*(11), 2359–2360. https://doi.org/10.1364/AO.8.002359

Eluszkiewicz, J. (1993). On the microphysical state of the Martian seasonal caps. *Icarus*, *103*, 13–48. https://doi.org/10.1006/icar.1993.1056

Eluszkiewicz, J., Moncet, J.-L., Titus, T. N., & Hansen, G. B. (2005). A microphysically-based approach to modeling emissivity and albedo of the Martian seasonal caps. *Icarus*, *174*(2), 524–534. https://doi.org/10.1016/j.icarus.2004.05.025

Forget, F. (1998). Mars CO_2 ice polar caps. In B. E. Schmidt (Ed.), *Solar system ices*, (pp. 477–507). B. V: Springer Science & Business Media.

Forget, F., Hansen, G. B., & Pollack, J. B. (1995). Low brightness temperatures of Martian polar caps: CO_2 clouds or low surface emissivity? *Journal of Geophysical Research*, *100*(E10), 21,219–21,234.

Forget, F., & Pollack, J. B. (1996). Thermal infrared observations of the condensing Martian polar caps: CO_2 ice temperatures and radiative budget. *Journal of Geophysical Research: Planets*, *101*(E7), 16,865–16,879. https://doi.org/10.1029/96je01077

France, J. L., King, M. D., & MacArthur, A. (2010). A photohabitable zone in the Martian snowpack? A laboratory and radiative-transfer study of dusty water–ice snow. *Icarus*, *207*(1), 133–139. https://doi.org/10.1016/j.icarus.2009.11.026

Genova, A., Goossens, S., Lemoine, F. G., Mazarico, E., Neumann, G. A., Smith, D. E., & Zuber, M. T. (2016). Seasonal and static gravity field of Mars from MGS, Mars Odyssey and MRO radio science. *Icarus*, *272*, 228–245. https://doi.org/10.1016/j.icarus.2016.02.050

Gillmann, C., Lognonné, P., Chassefière, E., & Moreira, M. (2009). The present-day atmosphere of Mars: Where does it come from? *Earth and Planetary Science Letters*, *277*(3–4), 384–393. https://doi.org/10.1016/j.epsl.2008.10.033

Hansen, C. J., Bourke, M., Bridges, N. T., Byrne, S., Colon, C., Diniega, S., et al. (2011). Seasonal erosion and restoration of Mars' northern polar dunes. *Science*, *331*(6017), 575–578. https://doi.org/10.1126/science.1197636

Hansen, C. J., Byrne, S., Portyankina, G., Bourke, M., Dundas, C., McEwen, A., et al. (2013). Observations of the northern seasonal polar cap on Mars: I. Spring sublimation activity and processes. *Icarus*, *225*(2), 881–897. https://doi.org/10.1016/j.icarus.2012.09.024

Hansen, C. J., Thomas, N., Portyankina, G., McEwen, A., Becker, T., Byrne, S., et al. (2010). HiRISE observations of gas sublimation-driven activity in Mars' southern polar regions: I. Erosion of the surface. *Icarus*, *205*(1), 283–295. https://doi.org/10.1016/j.icarus.2009.07.021

Hansen, G. B. (2005). Ultraviolet to near-infrared absorption spectrum of carbon dioxide ice from 0.174 to 1.8 μm. *Journal of Geophysical Research*, *110*(E1103). https://doi.org/10.1029/2005JE002531

Hayne, P. O., Paige, D. A., & Heavens, N. G. (2014). The role of snowfall in forming the seasonal ice caps of Mars: Models and constraints from the Mars Climate Sounder. *Icarus*, *231*, 122–130. https://doi.org/10.1016/j.icarus.2013.10.020

Hayne, P. O., Paige, D. A., Schofield, J. T., Kass, D. M., Kleinböhl, A., Heavens, N. G., & McCleese, D. J. (2012). Carbon dioxide snow clouds on Mars: South polar winter observations by the Mars Climate Sounder. *Journal of Geophysical Research: Planets*, *117*(E8), 1–23. https://doi.org/10.1029/2011je004040

Heldmann, J. L. (2005). Formation of Martian gullies by the action of liquid water flowing under current Martian environmental conditions. *Journal of Geophysical Research*, *110*(E5).

Heldmann, J. L., Carlsson, E., Johansson, H., Mellon, M. T., & Toon, O. B. (2007). Observations of Martian gullies and constraints on potential formation mechanisms. II. The northern hemisphere. *Icarus*, *188*(2), 324–344.

Heldmann, J. L., & Mellon, M. T. (2004). Observations of Martian gullies and constraints on potential formation mechanism. *Icarus*, *168*(2), 285–304.

Hudgins, D. M., Sandford, S. A., Allamandola, L. J., & Tielens, A. G. G. M. (1993). Mid- and far-infrared spectroscopy of ices—Optical constants and integrated absorbances. *Astrophysical Journal Supplement Series*, *86*(2), 713–870. https://doi.org/10.1086/191796

Kaufmann, E., & Hagermann, A. (2015). Penetration of solar radiation into pure and Mars-dust contaminated snow. *Icarus*, *252*, 144–149. https://doi.org/10.1016/j.icarus.2015.01.007

Kaufmann, E., & Hagermann, A. (2017). Experimental investigation of insolation-driven dust ejection from Mars' CO_2 ice caps. *Icarus*, *282*, 118–126. https://doi.org/10.1016/j.icarus.2016.09.039

Kieffer, H. H. (2000), Annual punctuated CO_2 slab-ice and jets on Mars, in Mars Polar Science, edited, p. 4095.

Kieffer, H. H. (2007). Cold jets in the Martian polar caps. *Journal of Geophysical Research*, *112*(E8). https://doi.org/10.1029/2006je002816

Kieffer, H. H., Christensen, P. R., & Titus, T. N. (2006). CO_2 jets formed by sublimation beneath translucent slab ice in Mars' seasonal south polar ice cap. *Nature*, *442*(7104), 793–796. https://doi.org/10.1038/nature04945

Kieffer, H. H., Titus, T. N., Mullins, K. F., & Christensen, P. R. (2000). Mars south polar spring and summer behavior observed by TES: Seasonal cap evolution controlled by frost grain size. *Journal of Geophysical Research*, *105*(E4), 9653. https://doi.org/10.1029/1999je001136

Kuroda, T., Medvedev, A. S., Kasaba, Y., & Hartogh, P. (2013). Carbon dioxide ice clouds, snowfalls, and baroclinic waves in the northern winter polar atmosphere of Mars. *Geophysical Research Letters*, *40*(8), 1484–1488. https://doi.org/10.1002/grl.50326

Langevin, Y., Bibring, J. P., Montmessin, F., Forget, F., Vincendon, M., Douté, S., et al. (2007). Observations of the south seasonal cap of Mars during recession in 2004–2006 by the OMEGA visible/near-infrared imaging spectrometer on board Mars Express. *Journal of Geophysical Research*, *112*(E8).

Langevin, Y., Doute, S., Vincendon, M., Poulet, F., Bibring, J. P., Gondet, B., et al. (2006). No signature of clear CO_2 ice from the 'cryptic' regions in Mars' south seasonal polar cap. *Nature*, *442*(7104), 790–792. https://doi.org/10.1038/nature05012

Li, W., Stamnes, K., Chen, B., & Xiong, X. (2001). Snow grain size retrieved from near-infrared radiances at multiple wavelengths. *Geophysical Research Letters*, *28*(9), 1699–1702. https://doi.org/10.1029/2000gl011641

Libois, Q., Picard, G., Dumont, M., Arnaud, L., Sergent, C., Pougatch, E., et al. (2014). Experimental determination of the absorption enhancement parameter of snow. *Journal of Glaciology*, *60*, 714–724.

Libois, Q., Picard, G., France, J. L., Arnaud, L., Dumont, M., Carmagnola, C. M., & King, M. D. (2013). Influence of grain shape on light penetration in snow. *The Cryosphere*, *7*, 1803–1818.

Mangan, T. P., Salzmann, C. G., Plane, J. M. C., & Murray, B. J. (2017). CO_2 ice structure and density under Martian atmospheric conditions. *Icarus*. https://doi.org/10.1016/j.icarus.2017.03.012

Martínez, G. M., Renno, N. O., & Elliott, H. M. (2012). The evolution of the albedo of dark spots observed on Mars polar region. *Icarus*, *221*(2), 816–830. https://doi.org/10.1016/j.icarus.2012.09.008

Matson, D. L., & Brown, B. H. (1989). Solid-state greenhouses and their implications for icy satellites. *Icarus*, *77*, 67–81.

Matsuo, K., & Heki, K. (2009). Seasonal and inter-annual changes of volume density of Martian CO_2 snow from time-variable elevation and gravity. *Icarus*, *202*(1), 90–94.

Mitrofanov, I. G., Zuber, M. T., Litvak, M. L., Boynton, W. V., Smith, D. E., Drake, D., et al. (2003). CO_2 snow depth and subsurface water-ice abundance in the Northern Hemisphere of Mars. *Science*, *300*, 2081–2084.

Möhlmann, D. T. F. (2010, 207). Temporary liquid water in upper snow/ice sub-surfaces on Mars? *Icarus*, 140–148. doi.org/10.1016/j.icarus.2009.11.013

Nash, C., & Bourke, M. (2015). *Southern hemisphere sand furrows: Spatial patterning and implications for the cryo-venting process*. Vienna, Austria, Copernicus: EGU General Assembly.

Perovich, D. K. (1996), The optical properties of sea ice, in Monograph 96–1, Edited, Office of Naval Research.

Pilorget, C., Edwards, C. S., Ehlmann, B. L., Forget, F., & Millour, E. (2013). Material ejection by the cold jets and temperature evolution of the south seasonal polar cap of Mars from THEMIS/CRISM observations and implications for surface properties. *Journal of Geophysical Research: Planets*, *118*(12), 2520–2536. https://doi.org/10.1002/2013je004513

Pilorget, C., & Forget, F. (2016). Formation of gullies on Mars by debris flows triggered by CO_2 sublimation. *Nature Geoscience*, *9*(1), 65–69.

Pilorget, C., Forget, F., Millour, E., Vincendon, M., & Madeleine, J. B. (2011). Dark spots and cold jets in the polar regions of Mars: New clues from a thermal model of surface CO_2 ice. *Icarus*, *213*(1), 131–149. https://doi.org/10.1016/j.icarus.2011.01.031

Piqueux, S., Byrne, S., & Richardson, M. I. (2003). Sublimation of Mars's southern seasonal CO_2 ice cap and the formation of spiders. *Journal of Geophysical Research*, *108*(E8). https://doi.org/10.1029/2002je002007

Piqueux, S., & Christensen, P. R. (2008). North and south subice gas flow and venting of the seasonal caps of Mars: A major geomorphological agent. *Journal of Geophysical Research*, *113*(E6). https://doi.org/10.1029/2007je003009

Piqueux, S., Kleinböhl, A., Hayne, P. O., Heavens, N. G., Kass, D. M., McCleese, D. M., et al. (2016). Discovery of a widespread low-latitude diurnal CO_2 frost cycle on Mars. *Journal of Geophysical Research: Planets*, *121*.

Portyankina, G., Hansen, C. J., & Aye, K.-M. (2017). Present-day erosion of Martian polar terrain by the seasonal CO_2 jets. *Icarus*, *282*, 93–103. https://doi.org/10.1016/j.icarus.2016.09.007

Portyankina, G., Markiewicz, W. J., Thomas, N., Hansen, C. J., & Milazzo, M. (2010). HiRISE observations of gas sublimation-driven activity in Mars' southern polar regions: III. Models of processes involving translucent ice. *Icarus*, *205*(1), 311–320. https://doi.org/10.1016/j.icarus.2009.08.029

Portyankina, G., Merrison, J., Iversen, J. J., Yoldi, Z., Hansen, C. J., Aye, K. M., et al. (2018). Laboratory investigations of the physical state of CO_2 ice in a simulated Martian environment. *Icarus*. https://doi.org/10.1016/j.icarus.2018.04.021

Portyankina, G., Pommerol, A., Aye, K.M., Thomas, N., Mattson, S. and Hansen, C.J., 2013, Influence of small scale topography on early spring activity in Martian polar areas. An example study based on DEM of Inca City region. In: 2013 European Planetary Science Congress (Abstract 2013–410).

Quirico, E., & Schmitt, B. (1997). Near-infrared spectroscopy of simple hydrocarbons and carbon oxides in solid N_2 and as pure ices: Implications for triton and Pluto. *Icarus*, *127*, 354–378.

Röttger, K., Endriss, A., Ihringer, J., Doyle, S., & Kuhs, W. F. (2012). Lattice constants and thermal expansion of H_2O and D_2O ice Ih between 10 and 265 K. *Addendum, Acta Crystallographica. Section B, Structural Science*, *68*(Pt 1), 91. https://doi.org/10.1107/S0108768111046908

Schneider, C. A., Rasband, W. S., & Eliceiri, K. W. (2012). NIH image to ImageJ: 25 years of image analysis. *Nature Methods*, *9*(7).

Schwamb, M. E., Aye, K.-M., Portyankina, G., Hansen, C. J., Allen, C., Allen, S., et al. (2018). Planet four: Terrains—Discovery of araneiforms outside of the south polar layered deposits. *Icarus*, *308*, 148–187. https://doi.org/10.1016/j.icarus.2017.06.017

Schwerdtfeger, P., & Weller, G. E. (1977). Radiative heat transfer processes in snow and ice. *Antarctic Research Series*, *25*. https://doi.org/10.1029/AR025p0035

Smith, D. E., Zuber, M. T., & Neumann, G. A. (2001). Seasonal variations of snow depth on Mars. *Science*, *294*(5549), 2141–2146. https://doi.org/10.1126/science.1066556

Smith, P. H., Tamppari, L. K., Arvidson, R. E., Bass, D., Blaney, D., Boynton, W. V., et al. (2009). H_2O at the Phoenix landing site. *Science*, *325*, 58–61.

Spiga, A., Hinson, D. P., Madeleine, J. B., Navarro, T., Millour, E., Forget, F., & Montmessin, F. (2017). Snow precipitation on Mars driven by cloud-induced night-time convection. *Nature Geoscience*, *10*, 652–657.

Thomas, P. C., Calvin, W. M., Gierasch, P., Haberle, R., James, P. B., & Sholes, S. (2013). Time scales of erosion and deposition recorded in the residual south polar cap of Mars. *Icarus*, *225*(2), 923–932. https://doi.org/10.1016/j.icarus.2012.08.038

Thomas, P. C., James, P. B., Calvin, W. M., Haberle, R., & Malin, M. C. (2009). Residual south polar cap of Mars: Stratigraphy, history, and implications of recent changes. *Icarus*, *203*(2), 352–375. https://doi.org/10.1016/j.icarus.2009.05.014

Thomas, P. C., Malin, M., Edgett, K. S., Carr, M. H., Hartmann, W. K., Ingersoll, A. P., et al. (2000). North-south geological differences between the residual polar caps on Mars. *Nature*, *404*.

Thomas, P. C., Malin, M. C., James, P. B., Cantor, B. A., Williams, R. M. E., & Gierasch, P. (2005). South polar residual cap of Mars: Features, stratigraphy, and changes. *Icarus*, *174*(2), 535–559. https://doi.org/10.1016/j.icarus.2004.07.028

Warren, S. G. (1986). Optical constants of carbon dioxide ice. *Applied Optics*, *25*(16), 2650–2674.